Atomic resolution with high-eigenmode tapping mode atomic force microscopy

N. Severin,[1] A. R. Dzhanoev,[2] H. Lin,[1] A. Rauf,[1,*] S. Kirstein,[1] C.-A. Palma,[3,1] I. M. Sokolov,[1,†] and J. P. Rabe[1,‡]

[1]*Department of Physics and IRIS Adlershof, Humboldt-Universität zu Berlin, Newtonstr. 15, 12489 Berlin, Germany*

[2]*Faculty of Physics, M. V. Lomonosov Moscow State University, Moscow 119992, Russia*

[3]*Institute of Physics, Chinese Academy of Sciences, P.O. Box 603, Beijing 100190, China*

(Received 4 September 2021; accepted 14 April 2022; published 24 May 2022)

Atomic surface structure imaging is instrumental for the understanding of surface-related phenomena. Here, we show that conventional tapping mode atomic force microscopy with high cantilever eigenmodes and subnanometer amplitudes allow routine atomic imaging at atmospheric pressures. We identify the reasons for failure of atomic resolution imaging employing low eigenmodes. Strong tip-surface interactions cause significant differences between the oscillatory behaviors of the inclination of the cantilever as detected by conventional instruments and of the vertical position of the tip, which prevents correct functioning of instrumental feedback control loops. However, high effective spring constants of high eigenmodes make it possible to overcome the problem. Furthermore, the combination of high effective elastic constants of high cantilever eigenmodes with the high flexibility of the cantilever substantially enhances the imaging stability, thereby universally allowing atomic imaging of solid surfaces in gaseous environments and at elevated temperatures. Demonstrated imaging examples include single sulfur vacancies at the surface of MoS_2 crystals imaged at temperatures ranging from room temperature to 250°C and potassium ions on hydrophilic and highly adhesive muscovite mica surfaces. Moreover, the high imaging stability allows knocking atoms off the MoS_2 surface by hard tapping, indicating the potential for ultrahigh resolution lithography.

DOI: 10.1103/PhysRevResearch.4.023149

I. INTRODUCTION

The invention of the atomic force microscope (AFM) more than three decades ago revolutionized surface analyses [1]. The AFM remains one of the most popular tools for the investigation of surfaces from ångstrom to micron scales in variable environments, most frequently in air. In its conventional design, AFM employs a sharp tip attached to a flexible cantilever. Monitoring the deflection of the cantilever is employed to evaluate the interaction force between the tip apex and a surface and to maintain this force constant during imaging by adjusting the cantilever-surface distance. As it was foreseen already in Ref. [1], it should be possible to resolve atomic features of surfaces provided that the forces acting between the front atom of the apex of the tip and surface atoms can be measured and kept small. While the required force sensitivity is routinely achieved nowadays, obtaining atomic resolution in AFM is still an issue, particularly in air. The problem here is that the contribution of the interaction between the front atom of the apex of the tip and surface atoms, which could give the atomic resolution, should be separated from all other interactions. The possibility of such a separation depends on the surface and on the mode of operation of the AFM. For example, contact mode, which uses the deflection of the cantilever as a feedback parameter, can reproduce the periodic structure of crystal surfaces but does not unambiguously reveal single-atom defects known to exist on the surfaces. A common explanation for this phenomenon invokes the assumption that, in contact mode, the apex of the tip becomes flattened by the adhesion forces, and the atoms of the apex of the tip adapt their periodicity to that of the substrate in contact mode [2,3].

The development of *tapping*, called also *amplitude modulation* (AM) or *intermittent contact mode*, largely broadened the use of force microscopy [4]. In tapping mode, the cantilever is driven at or close to its resonance frequency. The tip-sample distance is controlled by keeping the amplitude of the oscillations of the cantilever constant, with amplitudes typically >10 nm. Such oscillation amplitudes make it possible to overcome the short-range adhesion forces. In most of situations, the lateral resolution of AFM is worse than atomic also in tapping mode, with the exception of imaging in liquids discussed further below. Imaging with large amplitudes, albeit with frequency used as a feedback parameter keeping the tip-surface force constant, permits to achieve atomic resolution on reactive surfaces in ultrahigh vacuum (UHV). This was possible due to extremely large forces of bond forming between the tip apex and surface dangling bonds [5,6], which permits to obtain atomic resolution by scanning with large

*Present address: Park Systems Europe GmbH, Schildkrötstraße 15, 68199 Mannheim, Germany.

†sokolov@physik.hu-berlin.de

‡rabe@physik.hu-berlin.de

oscillation amplitudes (∼30 nm in Ref. [5]), considerably above the atomic scale. Obtaining atomic resolutions on nonreactive surfaces requires smaller oscillation amplitudes of the order of the typical decay length of the short-range repulsive component of the interatomic force, in practice, amplitudes <1 nm [7]. Thus, achieving atomic resolution for such surfaces is only possible when both the mean tip-to-surface distance and the oscillation amplitude of the tip are on the atomic scale, staying within the range of repulsive surface-tip interactions.

Up to now, imaging with subnanometer amplitudes and atomic resolution, respectively, can be routinely achieved on nonreactive surfaces under specific conditions only: in UHV and in liquids [7,8]. Imaging in UHV is typically done with stiff tuning forks (qPlus sensors [9]) with frequency as a feedback parameter. Imaging in liquids can be done with rather soft cantilevers in tapping mode. Achieving atomic resolution under ambient conditions, or more generally under ambient pressures in gas environments, is more difficult [10]. Claims of atomic resolution images showing perfect crystal lattices were proven later to be artifacts of tip flattening due to large tip-surface forces, like the ones discussed for the contact mode above [2,3]. An instructive analogy to understand this artifact is pulling a perfect eggcarton over another one with one of the pins missing. The missing pin cannot be identified by the perfect eggcarton sliding over the defected one, even though the lattice can be identified. Such images were called pseudo-atomic or lattice resolution images [10]. That is, to claim a truly atomic resolution, one needs to show imaging of atomic-scale defects.

To study relevant processes, it is often desired to image samples on the atomic scale under ambient pressures in gas environments. Publications showing atomic or nearly atomic resolutions in such environments are limited. It has been shown that near-atomic resolution on polymer samples can be achieved with torsional and bimodal tapping modes [11–13]. However, AFM imaging in tapping mode at ambient conditions with conventional cantilevers driven at their first eigenmode does not routinely provide atomic resolution because the oscillations of the tip with subnanometer amplitudes become unstable when the tip apex is brought close enough to a surface. The instability has been attributed to large adhesion forces caused by the formation of a water meniscus from a water film, typically covering surfaces under ambient conditions [14,15]. Other contributions may stem from surface contaminations. A remedy against instabilities was found in using considerably stiffer qPlus sensors (tuning forks) with cantilever stiffnesses typically >1 kN/m, possibly extending the routine UHV imaging to ambient [16]. This permitted to overcome the amplitude instabilities also under ambient conditions and made imaging with subnanometer amplitudes possible [17]. It was even possible to image an ambient water film coating the surface [16,17]. However, we are aware of only a few papers which published original data on atomic-scale resolution under ambient conditions with qPlus sensors since then [18–25].

Another remedy from such instabilities was found in the immersion of the AFM tip into a liquid. This reduces the tip-surface adhesion and prohibits meniscus formation. The technique allows for imaging with subnanometer amplitudes at solid-liquid interfaces [8,26], but at the same time, it reduces the applicability of the approach to situations when the existence and nature of the liquid phase are not prohibitive for the observation of structures of interest.

Employing high eigenmodes of conventional cantilevers has been shown to allow imaging with subnanometer amplitudes, improving thereby the resolution and allowing for manipulation of molecules [27–29]. These works, however, did not explain the reasons for the success of the approach and did not point to conditions under which the atomic resolution can be provided by high-eigenmode scanning. As we proceed to show, using higher eigenmodes for scanning with conventional cantilevers leads to stable imaging in tapping mode on a large variety of surfaces. We investigate the reason behind the enhanced stability of subnanometer amplitudes of high cantilever eigenmodes and show how and at which conditions subnanometer amplitudes can be used for achieving atomic resolution with a conventional AFM appliance. For this, we combine a theoretical analysis of the situation with experimental tests and demonstrations.

Here, we shortly discuss the physical situation. A cantilever can be modeled as a mechanical oscillator excited on its resonance frequency, which depends on the mode of the oscillation. The interaction of the cantilever and the surface enters the description in the form of an effective spring constant k^* of an additional spring, connecting the tip of the cantilever and the surface. The spring constant k^* is equal to the gradient of the tip-surface interaction force at the typical (average) position of the tip. The main parameter governing the behavior of the oscillation of the cantilever in close vicinity to the surface is the relation between k^* and the effective spring constant k_c of the cantilever [30], defining the new resonance frequency of a beam-surface system. At the first eigenmode of the cantilever beam [31], the effective spring constant k_c is of the order of the static spring constant of the cantilever beam.

Stable scanning is possible when the interaction with the surface does not bring the oscillations too far outside of the resonance domain. We will show that this condition is fulfilled when $Q\frac{k^*}{k_c} < 1$, with Q being the quality factor of the oscillator. For conventional cantilevers, the ratio $\frac{k^*}{k_c}$ is of the order of unity, and the quality factors in gaseous environments under atmospheric pressure are of the order of 10^2. Accordingly, the corresponding inequality is not fulfilled, the new resonance frequency is brought far outside of the resonance domain of a free oscillating beam, and the oscillations collapse. On the other hand, using hard cantilevers at their first eigenmode corresponds to large k_c and scanning in a liquid environment to small Q so that, under these conditions, imaging remains possible.

One may think that using a phase as a feedback parameter aiming at restoring the resonance might improve the situation and allow for stable imaging with conventional cantilevers. As we proceed to show, such a feedback control loop can hardly be implemented due to the fact that conventional instruments use laser beam deflection to detect the tip position of the cantilever. For strong interactions, the deflection of the beam, connected with the inclination of the end of the cantilever, gets out of phase with the displacement of the tip (as discussed

in Sec. III, see Fig. 4), preventing correct measurement and feedback control loop functioning, which are only possible when $\frac{k^*}{k_c} \ll 1$.

The effective spring constant k_n of the nth mode can be made very large by choosing n high enough [31]. The condition for stable scanning can always be fulfilled, and neither amplitude collapse nor dephasing prevent tracking of the displacement of the tip. For example, considerable dephasing at the third mode takes place for the values of k^* 30 times larger than for the first mode.

Moreover, the combination of a high effective spring constant with a high zero-frequency flexibility (i.e., low effective spring constant for the zero-frequency response) of the cantilever provides experimental advantages allowing for stable scanning in close contact with the surface. Thus, using relatively soft cantilevers relaxes the necessity for a precise tip-surface distance control and renders imaging at high eigenmodes with atomic resolution universally possible.

The structure of this paper is as follows: In Sec. II, we experimentally investigate the stability of cantilever oscillations for cantilevers excited at their first and higher eigenmodes; in Sec. III, we analyze the oscillation instabilities theoretically and answer why oscillations of the cantilevers are more stable when excited at high eigenmodes; in Sec, IV, we provide high-resolution imaging examples.

II. EXPERIMENTAL OBSERVATIONS

To better understand the stability of cantilever oscillations for cantilevers excited on their first and higher eigenmodes, we recorded phase, deflection, and amplitude curves for a conventional tapping mode cantilever excited at first and higher eigenmodes upon approach and then retraction from a MoS_2 surface. The distance-dependencies of amplitude and phase of oscillations recorded without and with active feedback control loops are shown in Figs. 1 and 2, respectively. The amplitudes of a freely oscillating cantilever were ∼0.8 nm for all eigenmodes. All sets of curves were offset along the x axis to match the force curve slopes. The red dotted vertical lines in Fig. 1 indicate maximum adhesion, i.e., the point where the tip-surface interactions become dominated by the repulsive forces; the black dotted line is displaced by 0.8 nm from the red one to illustrate the amplitude. The lines are guides for the eye. For the curves taken with no active feedback control loops, the detected amplitude of the cantilever driven at its first eigenmode becomes indiscernible before the tip apex starts sensing the repulsive forces. For the cantilever driven at its third eigenmode, the amplitudes remain discernable even for the cantilever being pushed onto the surface. Therefore, the amplitude of the third eigenmode can be used as a feedback parameter for imaging. Examples are shown in Sec. IV. Soft and hard tapping [Figs. 1(a), 1(b), and 5(a)] are achieved by using larger and smaller amplitude setpoints, respectively. The optimal imaging amplitude setpoint varied from tip to tip; the soft-hard sketch in Fig. 1 provides a rough imaging guide.

Figures 1(d)–1(f) show resonance curves taken with the tip retracted from the surface. The amplitude curve of the third eigenmode had often but not always satellite peaks. The amplitude curves were fitted with the solution for the driven damped harmonic oscillator:

$$A(\omega) = \frac{B}{\sqrt{\left(\omega_0^2 - \omega^2\right)^2 + \left(\frac{\omega_0}{Q}\omega\right)^2}}, \tag{1}$$

where B is a fitting parameter, ω_0 is the eigenfrequency, and Q is the quality factor. The fits are shown as green dashed lines. The Q factors from the fits of the curves shown in Figs. 1(d)–1(f) were $Q_1 = 372$, $Q_2 = 493$, and $Q_3 = 293$ for the first, second, and third eigenmodes, respectively. That is, the Q factors for all three eigenmodes are essentially quite high and show a nonmonotonic dependence on the mode number.

The plots shown in Fig. 1 evidence the difficulty to image with small amplitudes by driving the cantilever at its first eigenmode. Both phase and amplitude curves exhibit hystereses between approach and retract. Furthermore, the strong and nonmonotonous dependencies of both phase and amplitude on tip-surface separation render it practically impossible to use them as feedback parameters. Even more, the oscillation amplitudes become indiscernible well before the tip gets deflected upwards by the surface, which renders it impossible to map short-range repulsive forces.

In contrast, the same cantilever driven at its third eigenmode continues to oscillate, even when being deflected upwards by the repulsive forces, i.e., being pushed onto the surface. There is no hysteresis between approach and retract curves taken with and without active feedback control loops. The monotonous dependencies of amplitude, phase, and frequency on the z-piezo extension with no hysteresis between approach and retract curves render it possible to use both amplitude and phase as feedback parameters for imaging. The amplitude monotony makes imaging by exciting the high eigenmodes to be more stable than the conventional tapping mode, which is prone to hopping between attractive and repulsive imaging conditions [32]. The dependencies for the cantilever excited on its second eigenmode fall in between that of the first and third eigenmode. In the following section, we will discuss the curves taken with no active feedback control loops and then extend our discussion to the curves taken with active feedback control loops.

Figures 1(a)–1(c) display the behavior of the oscillations of the cantilever at different eigenmodes. As the tip approaches the surface, the phase curves for the first and second eigenmodes exhibit positive phase shifts, implying that the attractive forces between the tip and the surface are dominant. The third eigenmode is virtually insensitive to these weak attractive forces. For the first eigenmode, decreasing the distance to the surface leads to amplitude collapse accompanied by hysteresis between approaching and retracting the tip. For the second mode, the amplitude also decays quite rapidly when approaching the surface but shows virtually no hysteresis. However, the phase behavior in this mode is quite peculiar: the phase curve shows a sharp peak: the phase shift first grows >90° and then decays below this value. The average tip position corresponding to the peak is denoted by the black dotted vertical line. The red dotted line illustrates the largest deviation of the tip from its mean position, when this mean position corresponds to the black line. The red line coincides with the bottom of the deflection curve, so that the decay in the phase shift may be attributed to the growing

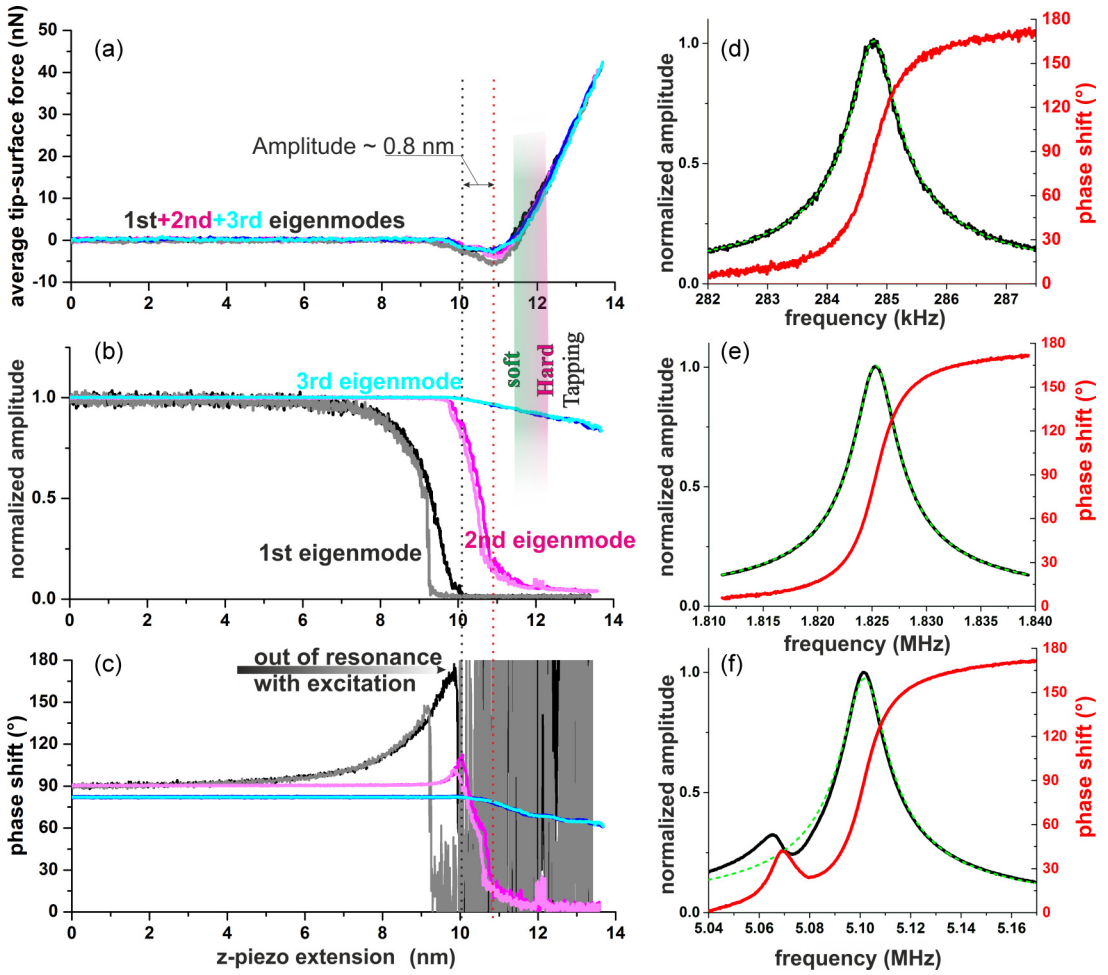

FIG. 1. Distance dependencies of (a) average tip-surface forces, (b) normalized deflection amplitudes, and (c) phase shifts between excitation and cantilever deflection. The data were recorded with a generic tapping mode cantilever (NSC15) excited at frequencies matching its first (black/gray curves), second (magenta/light magenta), and third (blue/light blue curves) eigenmodes of a freely oscillating cantilever. The tip was first approaching (black/magenta/blue curves) and then retracting (gray/light magenta/light blue curves) from the MoS_2 surface. The data were taken without active feedback control loops, i.e., excitation frequency and excitation amplitude remained constant. (d) First, (e) second, and (f) third eigenmode resonance curves taken with the same cantilever. The black and red curves show the amplitudes and phases, respectively. The green dashed line shows the fits with the solution for the driven damped harmonic oscillator. (c) As evident in the phase signal, the first mode goes out of resonance as the tip approaches the sample, while the third eigenmode excitation remains near resonance. The soft/hard tapping bar in (a) and (b) shows roughly the third eigenmode amplitude setpoints used to produce images shown in Figs. 5 and 6 in soft tapping and to knock off atoms in hard tapping. The "soft" imaging is achieved at ∼0 force. The two vertical dotted lines in (a)–(c) are guides for the eye, illustrating the oscillation amplitude of ∼0.8 nm.

contribution of repulsive forces. On its decaying branch, the phase curve again passes the value of 90° which, when neglecting losses, would assume that the frequency is now back to resonance. This behavior of phase is, however, not reflected in the amplitude of oscillations, which monotonically decays. The behavior of both the phase shift and the amplitude for the third eigenmode correspond to a relatively slow monotonic decay. Our theoretical discussion in Sec. III will provide explanations for the behaviors seen.

III. THEORETICAL DISCUSSION

A. A basic lumped model of the force curves taken without active feedback control loops

The drastic reduction of the amplitude of the first-eigenmode oscillation for small tip-surface distances, as seen in Fig. 1(b), may have two physical causes. One is the considerable shift of the cantilever eigenfrequency due to the tip-surface interaction, which brings the oscillator out of resonance with the excitation. The second cause may be strong amplitude damping by dissipative interactions with the surface, as might be suggested by the results of Fig. 2(c). There is reason to consider the first cause as the major contribution and the second one as unlikely.

The high stability of the cantilever oscillation close to the surface, when excited in its third eigenmode, implies insignificant contributions of dissipative interactions with the surface in the corresponding regime. If the dissipation is weak for the third eigenmode but strong for the first, one should assume that the dissipation into the surface must rapidly decay with frequency. Such a dependence cannot be excluded *a priori*, but it is not reproduced by simple models, like the

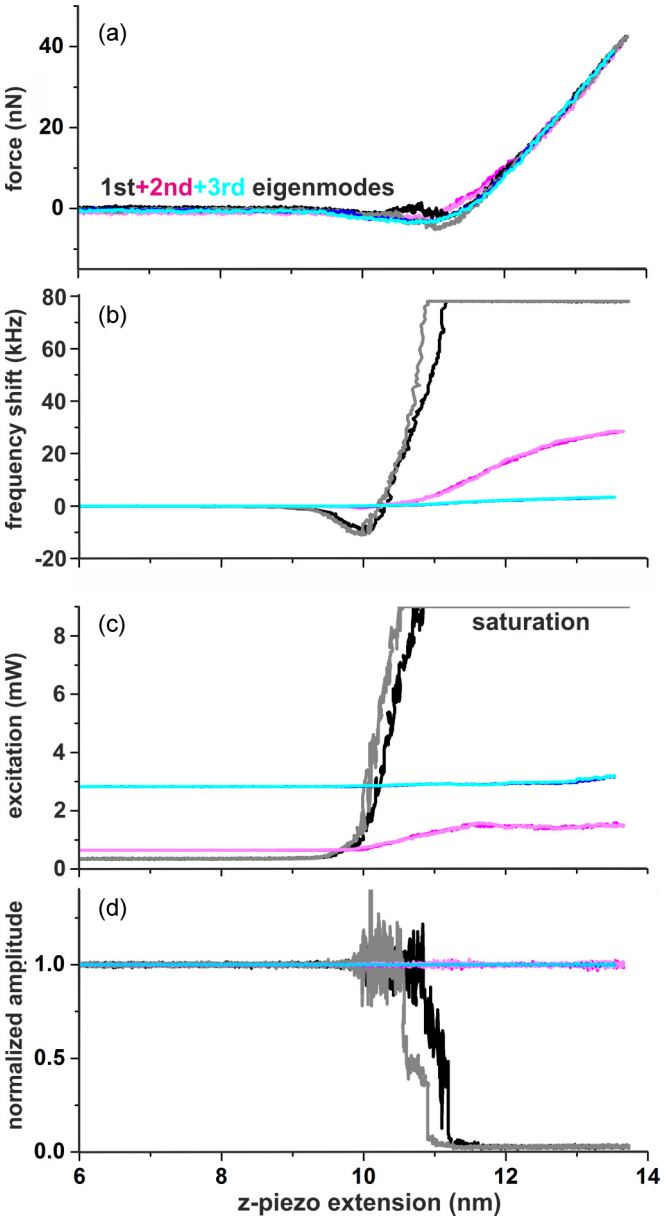

FIG. 2. The distance dependences of (a) average forces, (b) frequency shifts, (c) excitation powers, and (d) normalized amplitudes for first (black/gray curves), second (magenta/light magenta curves), third eigenmodes (blue/light blue curves). The color coding is the same as in Fig. 1. Two feedback control loops were on: The first feedback control loop kept the excitation frequency on resonance by keeping the phase shift ∼90°, the second feedback control loop kept the amplitude constant by adjusting the excitation power. Such feedback control loops are typically employed in the frequency modulation (FM) atomic force microscopy (AFM). The frequency shift near the surface reduces from >70 kHz to a few kilohertz from first to third eigenmode. Additionally, excitation power required to keep the inclination amplitude reaches hardware saturation for the first eigenmode. We discuss that it is a sort of an instrumental artifact (see discussion)—for strong tip-surface interactions, with the inclination amplitude not being useful as a feedback parameter. These results make it evident that the cantilever oscillation when excited at its third eigenmode is more stable than at its first eigenmode.

Kelvin-Voigt model of interaction between the tip and the surface [30], or by standard mechanisms of internal dissipation in the bulk, which suggest the opposite behavior (unless one makes additional *ad hoc* assumptions). Excluding this mechanism, we however have to seek an alternative explanation for the findings in Fig. 2. As we proceed to show, such an explanation is indeed found in the analysis of the measurement procedure, and the situation can be rationalized assuming the tip-surface interactions to be purely conservative. The dissipation into the sample can be easily included into the theory but is not necessary to pinpoint the main effect.

Let us discuss the linearized model of the tip-surface interaction, and let us assume that this interaction can be modeled by an additional spring, with the spring constant k^* being equal to the gradient of the surface forces [33]. This is a rather rough assumption, leaving out all possible nonlinear effects, which might be of importance [33]. Nevertheless, this assumption will allow us to discuss the oscillatory behavior of the cantilevers close to the surface, and it describes our findings at least qualitatively.

We start from a lumped, point-mass model of a system: a damped harmonic oscillator. The oscillator has a resonance frequency being the eigenfrequency of the mode modeled. The parameters of this effective oscillator for different modes are discussed in Ref. [34], which shows how the effective parameters of the oscillator should be connected with the geometry of the cantilever and the mode number: this, namely, should be done by matching the kinetic and potential energy of the cantilever and the virtual work of inertial forces. The calculations then show that, within such a lumped description, the mass of the effective oscillating particle stays independent from the mode number. It is proportional to the total mass of the cantilever, while the dependence of the eigenfrequency of oscillations on the mode number is solely described by changing the effective spring constant of the oscillator for the nth mode, showing a strong dependence on the mode number.

The interaction between the tip and surface is modeled by an additional spring with elastic constant k^*, which shifts the frequency of the oscillator. The new resonance frequency is now one of a harmonic oscillator with spring constant $(k_c + k^*)$ [33]. The frequency shift between the resonance frequency f_0 of the freely oscillating cantilever and the resonance frequency of the cantilever interacting with the surface is then [33] $\Delta f \approx -\frac{f_0}{2k_c}k^*$ or $\Delta f/\Delta f_{\mathrm{FWHM}} \approx -Q\frac{k^*}{2k_c}$, with cantilever quality factor $Q \equiv \frac{f_0}{\Delta f_{\mathrm{FWHM}}}$ and Δf_{FWHM} being the width of the resonance peak. The second equality implies that the condition $Q\frac{k^*}{k_c} \lesssim 1$ must hold for the excitation to remain within the resonance peak. If the opposite is true, the amplitude of oscillations reduces considerably, and for large detuning, it may fall beyond the limit at which it can be detected. The spring constants of conventional tapping mode cantilevers lie roughly in the range from a few to a hundred Newtons per meter. The gradients of typical tip-surface forces fall into the same range [35]. Therefore, the tip-surface interaction readily shifts the first eigenmode frequency far out of the resonance with excitation, considering typical cantilever Q factors of $Q \gtrsim 10^2$ in air [36]. We propose this to be the main reason for the amplitude collapse for the cantilevers excited on their first eigenmodes. This also partly explains the stability of

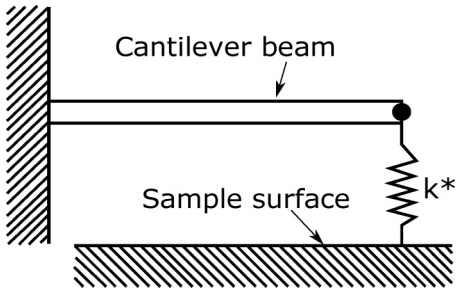

FIG. 3. Sketch of the model of an atomic force microscopy (AFM) clamped spring-coupled cantilever with a uniform cross-section.

oscillations in liquid surroundings: it is not only due to the elimination of the meniscus formation but also due to simply reducing the oscillator quality factor Q. Since the effective spring constants for the higher eigenmodes are considerably higher (the estimates of Ref. [31] give $k_2 \approx 40k_1$ and $k_3 \approx 300k_1$ for a simple rectangular cantilever), the amplitude does not collapse, the oscillations stay detectable, and imaging is possible.

The discussion of the lumped model above might suggest that applying a phase feedback control loop and keeping the excitation in resonance with the first eigenmode of the cantilever should stabilize the subnanometer amplitudes of tip oscillations, even if the tip is interacting with a surface, when the frequency shift gets considerable. However, as one readily infers from Fig. 2, this is not the case. As we proceed to show, applying feedback control loops when using conventional AFM appliances only makes the situation worse.

Analyzing the situation, we identified a further reason for the measured amplitude instability, now for measurements with active feedback control loops, which is of instrumental nature. Most commercial equipment detects cantilever inclination α instead of the z position of the tip and recalculate the latter from the former. In the following, we demonstrate that, while for a free oscillating cantilever, the z position of its tip and inclination change nearly in phase, and amplitudes of the z-tip motion A_z and of cantilever inclination A_α are proportional to each other, the situation with surface interactions may be vastly different. The z position of the tip and inclination move out of phase, and the phase shift may get large when the interaction gets stronger. To show this, we perform model calculations for a cantilever clamped on one end and connected to a surface with a spring with spring constant k^* on the other end (Fig. 3). Specifically, we calculate the phase shift between the z coordinate of the tip and the inclination of the free end of the cantilever for the case when the cantilever is excited on one of its eigenfrequencies.

B. A beam model for a cantilever

We adapt here the model detailed previously in Ref. [30] and depicted in Fig. 3. A brief description of the mechanical model is as follows. The cantilever is assumed to be a homogenous beam with a rectangular cross-section. It is clamped on one end ($x = 0$), and its other end has a coordinate $x = L$. The tip-surface interaction is linearized and modeled by a spring with the spring constant k^* connecting the tip at L with the surface. This model introduced in Ref. [30] is extended by introducing the damping and driving forces. The equation of motion of a driven cantilever beam is now

$$EI\frac{\partial^4 u}{\partial x^4} + \mu u_{tt} + \gamma u_t + EI\eta\frac{\partial}{\partial t}\left(\frac{\partial^4 u}{\partial x^4}\right) = h(x,t); \quad 0 < x\langle L,t\rangle 0, \tag{2}$$

where $u = u(x,t)$, x is the coordinate in the longitudinal direction of the cantilever, E is the Young's modulus of the material of the beam, ρ is its mass density, γ is the external damping coefficient, and η is the internal damping coefficient. For a beam of rectangular cross-section $A = ab$ with width a and thickness b, the area moment of inertia $I = ab^3/12$. The combination EI is the bending stiffness, and $\mu = \rho A$ is the mass per unit length. Here, the external damping term models Stokes' friction for the motion of the cantilever in ambient air (see, e.g., Ref. [37]), and the internal damping term follows from the Kelvin-Voigt model, for which the stress-strain relation is $\sigma = \varepsilon E + \eta\dot{\varepsilon}E$, where ε is the strain in the cantilever (see, e.g., Ref. [38]). The article in Ref. [39] devoted to a fractional variant of the model contains additional references to the normal approach. All other mechanisms of damping (say, acoustic emission) are neglected. The right-hand side of the equation models the driving force; the way it is introduced will be discussed later.

For the model in Fig. 3, the boundary condition at $x = 0$ is

$$u(0,t) = 0, \quad u_x(0,t) = 0, \tag{3}$$

and the boundary condition at $x = L$ reads

$$u_{xx}(L,t) = 0, \quad u_{xxx}(L,t) = \frac{k^*}{EI}u(L,t). \tag{4}$$

When putting down the last condition, we assume that the driving amplitude is small compared wih the oscillation amplitude of the free end of the cantilever. Note that, when $k^* \to 0$ (very soft spring) and $k^* \to \infty$ (very stiff spring), we obtain the boundary conditions that correspond to the clamped-free case and the clamped-pinned case, respectively.

1. Eigenmodes of oscillations without external driving

First, we study the undamped cantilever ($\gamma = 0,\ \eta = 0$) in the absence of external forcing $h(x,t) = 0$. In this case, the solution of Eq. (2) becomes separable in space and time, so that this solution can be put in a form

$$u(x,t) = \psi(\kappa,x)F(t), \tag{5}$$

with the time-dependent function $F(t)$ corresponding to a harmonic oscillation. The argument κ of $\psi(\kappa,x)$ is equal to $\kappa = k^*/k_c$ with $k_c = 3EIL^{-3}$ being the spring constant of the cantilever. The explicit use of this argument in Eq. (5) is necessary since the further results will be plotted as functions of this parameter. Under substitution of the solution in Eq. (5), Eq. (2) reduces to the equation (the eigenvalue problem) for $\psi(\kappa,x)$:

$$\frac{d^4\psi(\kappa,x)}{dx^4} = \beta^4\psi(\kappa,x); \quad 0 < x < L, \tag{6}$$

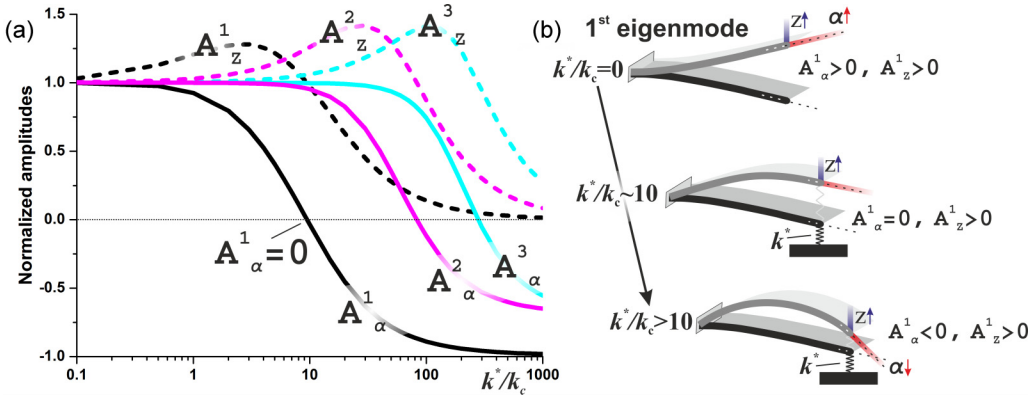

FIG. 4. We explain the instability of the first eigenmode cantilever deflection amplitudes with the shift of the eigenfrequency out of the resonance with the excitation due to tip-surface interactions (see also discussion). The shift out of the resonance is influenced by the changes in the shape of the oscillating cantilever. (a) Model calculations reveal that the cantilever inclination amplitudes (A^n_α) in the nth mode at the end of a rectangular cantilever undergo a transition from being in phase to being out of phase with the tip oscillation (A^n_z), as the tip-surface interactions (k^*) increase. Thus, neither phase nor cantilever inclination amplitude in the first eigenmode should be used as the feedback parameter for the strong tip-surface interactions. The large effective spring constant of the third eigenmode renders the detected cantilever amplitudes to be more stable. The sketch in (b) schematically illustrates the transition from in-phase to out-of-phase oscillations of tip position and cantilever inclination driven in resonance with its first eigenmode.

where the function $\psi(\kappa, x)$ must satisfy the appropriate boundary conditions. Inserting Eq. (5) into Eqs. (3) and (4) and eliminating the time dependence, we obtain boundary conditions similar in form to Eqs. (3) and (4), with the exception that $u(x,t)$ is replaced by $\psi(\kappa, x)$ and partial derivatives with respect to x by total derivatives with respect to x. Thus, the eigenfunctions for the model in Fig. 4 are

$$\psi(\kappa, x) = \cosh \beta x - \cos \beta x - D(\kappa, L)(\sin \beta x - \sinh \beta x), \tag{7}$$

with $D(\kappa, L)$ being

$$D(\kappa, L) = \frac{\alpha(\kappa)(\cosh \beta L - \cos \beta L) + \sin \beta L - \sinh \beta L}{\alpha(\kappa)(\sin \beta L - \sinh \beta L) + \cosh \beta L + \cos \beta L}, \tag{8}$$

where $\alpha(\kappa) = 3\kappa(\beta L)^{-3}$, $\kappa = k^*/k_c$, and eigenvalues βL for all the boundary conditions can be obtained by solving the (transcendental) characteristic equation:

$$1 + \cosh \beta L \cos \beta L + \alpha(\kappa)(\sin \beta L \cosh \beta L - \sinh \beta L \cos \beta L) = 0. \tag{9}$$

The relationship between eigenvalues and undamped eigenfrequencies is $\omega = \beta^2 \sqrt{EI\mu^{-1}}$. The eigenfunctions $\psi(\kappa, x)$, under proper normalization, build a complete orthonormal system of functions (see Appendix B), over which the solutions for the forced case will be expanded.

In Fig. 4(a), we show how the vertical displacement of the cantilever $\psi_n(\kappa, L)$ and its inclination [slope $\frac{\partial \psi_n(\kappa, x)}{\partial x}|_{x=L}$ at the free end] depend on κ for the first three eigenmodes (in the absence of damping). Here, n is the eigenmode number. To do so, we obtain the eigenvalues $\beta_n L$ by numerically solving the characteristic equation, Eq. (9), for different values of $\kappa = k^*/k_c$. For example, for the first three eigenmodes when $k^*/k_c = 1$, we have $\beta_1 L = 2.2135$, $\beta_2 L = 4.7234$, and $\beta_3 L = 7.86097$; more exemplary values can be found in table IV in Ref. [30]. Then we calculate the mode forms $\psi_n(\kappa, L)$ and plot the displacement of the cantilever end and inclination as a function of κ. Note that, for each mode n, there exists a value of κ_n at which the slope (inclination) changes its sign with respect to the position. Hence, for $k^*/k_c \geqslant \kappa_n$, the vertical position of the cantilever and the slope are shifted in phase by π relative to each other. The estimated numerical values of the corresponding κ_n are $\kappa_1 = 9.5$, $\kappa_2 = 83$, $\kappa_3 = 280$, and $\kappa_4 = 660$. Thus, the value of κ_n increases with the increase of the mode number n. Figures explicitly showing the form of the modes [i.e., the functions (κ, x)] can be found, e.g., in Ref. [34].

Before continuing to the discussion of the driven cantilever, we study the effect of damping to estimate the relative role of external and internal contributions at different frequencies. We start from the discussion of the eigenmodes of oscillations. The equation of motion Eq. (2) for the cantilever with damping and $h(x,t) = 0$ reads

$$u_{tt} + c^2 \frac{\partial^4 u}{\partial x^4} + \tilde{\gamma} u_t + c^2 \eta \frac{\partial}{\partial t}\left(\frac{\partial^4 u}{\partial x^4}\right) = 0; \quad 0 < x\langle L, t\rangle 0, \tag{10}$$

with $c^2 = EI\mu^{-1}$, and $\tilde{\gamma} = \gamma\mu^{-1}$. We seek the solution of Eq. (10) in the form

$$u(x,t) = u_0 \exp[i(\omega_n t - k_n x)]. \tag{11}$$

After substitution of Eq. (11) into Eq. (10), for each mode ω_n, we obtain

$$-\omega_n^2 + i\tilde{\gamma}\omega_n + i\eta c^2 \omega_n k_n^4 + c^2 k_n^4 = 0, \tag{12}$$

and

$$k_n^4 = \tilde{k}_n^4 \frac{1 - i\tilde{\gamma}\omega_n^{-1}}{1 + i\eta\omega_n}, \tag{13}$$

with $\tilde{k}_n^4 = \frac{\omega_n^2}{c^2}$ when $\gamma = 0$ and $\eta = 0$. From Eq. (13), we get

$$k_n = \tilde{k}_n\left[1 - i4^{-1}\left(\tilde{\gamma}\omega_n^{-1} + \eta\omega_n\right)\right] + \text{h.o.t.}, \tag{14}$$

when $\tilde{\gamma}\omega_n^{-1} \ll 1$ and $\eta\omega_n \ll 1$ with h.o.t. denoting the higher-order terms. Now we substitute Eq. (14) into Eq. (11) and obtain

$$u_0 \exp[i(\omega_n t - \tilde{k}_n x) - (\gamma_n + \eta_n)x], \tag{15}$$

where $\gamma_n = 4^{-1}\tilde{k}_n\tilde{\gamma}\omega_n^{-1}$, and $\eta_n = 4^{-1}\tilde{k}_n\eta\omega_n$. Thus, we have shown that the solution to Eq. (10) decays, and the measure of its decay is the imaginary part of k_n in Eq. (14). In the higher modes, the external damping ratios are

$$\gamma_n = \gamma_1 \frac{\omega_1}{\omega_n}, \tag{16}$$

and for the internal damping ratios, we obtain

$$\eta_n = \eta_1 \frac{\omega_n}{\omega_1}. \tag{17}$$

In our model, the damping can be specified as in Eqs. (16) and (17) with $\gamma_1 = 2^{-1}\tilde{\gamma}\omega_1^{-1}$ and $\eta_1 = 2^{-1}\eta\omega_1$—the first mode damping ratios in the cases of external and internal damping correspondingly. This implies that the external damping ratios for the higher modes decrease with increasing n, whereas the internal damping ratios increase with increasing n. Thus, the effect of the internal damping is strong at higher modes, and the effect of the external damping is strong at lower modes.

2. *Oscillations under external driving*

We turn to the discussion of the motion of the cantilever under external driving. The driving force is introduced by changing to a comoving frame of the clamped end of the cantilever. Let the clamped end of the cantilever be driven with amplitude A_0 at frequency ω. In a comoving frame of the end [where this is immobile and where thus the clamped boundary condition in Eq. (3) now applies], this creates a homogeneous force field $h(x,t) = A_0\omega^2\mu\cos\omega t\,\Theta(L-x) = a_0\Theta(L-x)\cos\omega t$ per unit length, with $\Theta(x)$ being the Heaviside function. The coordinate and the time dependencies in the force separate: $h(x,t) = f(x)g(t)$. The spatial part of the driving force $h(x,t) = f(x)g(t)$ is expressed in terms of the orthogonal cantilever functions [in Eq. (7)] as

$$f(x) = \sum_{n=1}^{\infty} f_n \psi_n(\kappa, x), \tag{18}$$

where

$$f_n = \frac{1}{L}\int_0^L \sqrt{\chi(\kappa)} f(x)\psi_n(\kappa, x)dx, \tag{19}$$

with $\chi(\kappa)$ being the normalization constant for the eigenfunctions (see Appendix B). The solution to Eq. (2) is given in the form

$$u(x,t) = \sum_{n=1}^{\infty} \psi_n(\kappa, x)v_n(t). \tag{20}$$

After the substitution of this equation into Eq. (2), for the time-dependent part of the solution $v_n(t)$, we obtain the set of uncoupled ordinary differential equations for the normal coordinates:

$$\ddot{v}_n + 2\zeta_n\omega_n\dot{v}_n + \omega_n^2 v_n = \mu^{-1} f\cos\omega t, \tag{21}$$

where $\zeta_n = \eta_n + \gamma_n = 2^{-1}\eta\omega_n + 2^{-1}\tilde{\gamma}\omega_n^{-1}$, and $f = a_0 f_n$. The general solution to this equation is

$$v_n(t) = B_n \exp(-\zeta_n\omega_n t)\cos\Omega t + C_n(\omega)\cos(\omega t + \varphi_n), \tag{22}$$

and for the steady state solutions (for $t \to \infty$) we have

$$v_n(t) = C_n(\omega)\cos(\omega t + \varphi_n), \tag{23}$$

where the amplitude is

$$C_n(\omega) = \frac{\mu^{-1}a_0 f_n}{\sqrt{\left(\omega_n^2 - \omega^2\right)^2 + 4\zeta_n^2(\omega_n\omega)^2}}, \tag{24}$$

and the phase is

$$\varphi_n = \tan^{-1}\frac{2\zeta_n\omega\omega_n^{-1}}{\omega^2\omega_n^{-2} - 1}. \tag{25}$$

Now by comparing the Eq. (24) with Eq. (1), we get the connection between the quality factor Q and the damping coefficients γ and η:

$$Q(\omega_n) = \frac{1}{2\zeta_n} = \frac{1}{2\eta_n + 2\gamma_n} = \frac{1}{\eta\omega_n + \gamma(\mu\omega_n)^{-1}}. \tag{26}$$

Finally, the solution to Eq. (2) for a cantilever driven at a frequency close (within the resonance domain) to the eigenfrequency of the nth mode of oscillation is

$$\begin{aligned} u(x,t) &= u_n(x,t) = \psi_n(\kappa, x)v_n(t) \\ &= \psi_n(\kappa, x)C_n(\omega)\cos(\omega t + \varphi_n). \end{aligned} \tag{27}$$

The analysis of Eqs. (24) and (25) reveals that the vibration of the cantilever lags behind the excitation. In the absence of the damping, the phase of the driven vibration changes discontinuously by π at $\omega = \omega_n$—the function $v_n(t)$ in Eq. (22) changes the sign, and in the presence of damping, this discontinuity is smoothed out. Note that Eq. (26) following from our model calculations suggests that the quality factor $Q(\omega_n)$ is a nonmonotonic function of the mode frequency ω_n, which might explain our experimental findings for the first three modes.

We illustrate in Fig. 4(b) that an increasing tip-surface interaction leads to out-of-phase oscillations of z and α. Moreover, the amplitudes of z-tip motion and cantilever inclination do not remain proportional to each other. For instance, for intermediate tip-surface interactions, the amplitude of cantilever inclination A_α becomes zero, while the tip continues to oscillate.

Thus, using neither phase nor amplitude of inclination as feedback parameters would guarantee stable imaging at low eigenmodes. Even if we keep the detected inclination amplitude constant in the frequency modulated (FM) imaging mode, the real tip oscillation amplitude might substantially exceed the nanometer amplitudes needed to obtain the atomic resolution. This explains the findings of Fig. 2(d), where the excitation may essentially power large-amplitude oscillations

of the cantilever, which cannot be detected because the inclination amplitude stays small. Thus, both AM and FM imaging modes significantly impair atomic resolution for cantilevers excited on their first eigenmode under a conventional laser-deflection measurement constellation. The case with higher eigenmodes is much less dramatic since, here, the value of k^*/k_c is considerably smaller than unity.

C. Lessons from the theoretical analysis

We start our discussion with the coarse model detailed in Sec. III A. Increasing the cantilever spring constant reduces $Q\frac{k^*}{k_n}$ and the relative shift of the resonance frequency, respectively. For a conventional rectangular cantilever, the effective spring constant can be increased significantly by employing higher eigenmodes. For example, for the third eigenmode, the effective spring constant k_3 is 308 times larger than k_1 of the first eigenmode. Thus, k_3 of the cantilevers used to acquire the curves shown in Fig. 2 is $\sim$12.3 kN m^{-1}, which is an order of magnitude larger than the spring constant of quartz tuning forks [21]. The high effective spring constant of the third eigenmode renders the tip oscillation effectively insensitive to long-range weak attractive forces, the phase shift noticeably changes only when the tip gets close enough to the surface to sense the steep repulsive forces, and the excitation remains within the resonance peak. Thus, both amplitude and phase depend monotonically on the tip-surface separation. Using even higher eigenmodes should allow imaging of surfaces with arbitrary k^*. Furthermore, the average tip-surface force (Figs. 1 and 2) for a cantilever excited on its high eigenmodes is defined by the rather soft zero-frequency spring constant, which is almost identical to k_1. This makes it easier to keep the tip-surface forces below the damage threshold of tip and surface (Fig. 2). Using stiff cantilevers with k_1 on the order of 10 kN m^{-1} should hypothetically allow imaging with subnanometer amplitudes and correspondingly atomic resolution under ambient conditions. However, a higher stiffness of cantilevers imposes also more constraints on the precision of the tip-sample distance control, making it challenging to employ stiff cantilevers for uneven samples. Moreover, imaging with subnanometer amplitudes is expected to remain stable in a broad range of temperatures. The damping of cantilever vibrations, and thus the Q factor, is largely dominated by the internal damping, and the viscous damping of the cantilever environment. Cantilever material properties and the effective spring constants are not expected to vary largely over a broad temperature range, and thus, high-resolution imaging should be possible at variable temperatures [40].

IV. ATOMIC RESOLUTION IN HIGH-EIGENMODE AFM

The visualization of single atom defects is considered a direct confirmation of imaging to provide true atomic resolution. As a test sample, we selected natural crystals of MoS_2, which is known to exhibit atomic defects on its surface [43], and we imaged it with both tapping mode AFM and scanning tunneling microscopy (STM; Fig. 5 and Supplemental Material [41]). Imaging in tapping mode AFM was carried out with subnanometer amplitudes by exciting high eigenmodes and readily revealed a periodic hexagonal pattern with the unit cell matching the one expected for the sulfur atoms on the surface of MoS_2 [44]. Most of the AFM images also revealed point defects. The contrast of the defects varied from tip to tip, and it could also change during imaging (see, e.g., the Supplemental Material [41]), possibly due to the differences in tip apex structure. The image in Fig. 5(a) exemplifies a strong contrast. Imaging with some tips resulted in double and sometimes even multiple tip artifacts (Supplemental Material [41]). The contrast variation and the formation of the double tip artifacts are difficult to discuss due to unknown tip structures and possible passivation of the atomic defects by ambient molecules [45]. However, both AFM and STM imaging of MoS_2 reveal the same defect density, which we consider direct proof that the imaging can provide true atomic resolution. The high amplitude stability allowed us to tap the surfaces harder. Even though the hard tapping resulted in most cases in tip damage and correspondingly inferior image quality, it was possible to image knocking off the atoms with one diamond tip (AD-40-SS, fourth eigenmode).

Next, we selected graphite for its smaller unit cell to test the resolution limits [Fig. 5(b), NSC15, third eigenmode]. Resolving the honeycomb structure of a graphite surface allows us to hypothesize that the lateral resolution we obtain here is approaching the C-C bond length, i.e., the lateral resolution is better than 2 Å. To demonstrate that the imaging by exciting high eigenmodes inherits the capability of tapping mode to image soft structures, we imaged a layer of arachidic acid molecules on a graphite surface [Fig. 5(c), NSC15, third eigenmode]. The individual molecules, self-assembled into lamellae, could be readily resolved, like in STM at solid-liquid interfaces [46]. The packing can be assigned to an alternating arrangement of the head groups, as also observed by STM [42]. To demonstrate that also corrugated surfaces can be imaged with atomic resolution, we imaged a MoS_2 monolayer grown on a substrate with a roughness on the nanometer scale [Fig. 5(d), qp-fast long, third eigenmode] [47].

To test the imaging stability on hydrophilic surfaces, we imaged muscovite mica under dry nitrogen (Fig. 6, qp-fast long, third eigenmode). Mica is a layered mineral with an archetypical hydrophilic surface [48]. The aluminosilicate layers of mica bear negative charge on their surfaces. The layers are held together by the interlayer potassium cations. Roughly half of the cations remain on either side upon cleavage of mica [49]. Imaging of mica under dry nitrogen readily reveals its unit cell, as one can see in the fast Fourier transforms of the images (white arrows in the inset of Fig. 6). Moreover, the images reveal patterns of irregularly distributed dots, and it is tempting to attribute them to potassium ions. Unfortunately, it was rather difficult to prove the stability of the patterns to answer the question whether the K^+ ions become displaced by the AFM tip during imaging. We attempted to image mica a number of times, and in most imaging sessions, we could resolve patterns like that shown in Fig. 6. However, the image quality in most attempts did not remain stable enough to acquire two subsequent high-resolution images on the same area. Figure 6 shows one successful attempt to take two subsequent images on one area. Images (a) and (b) were taken with the slow scan directions downward and upward, respectively. Careful inspection of the images reveals a

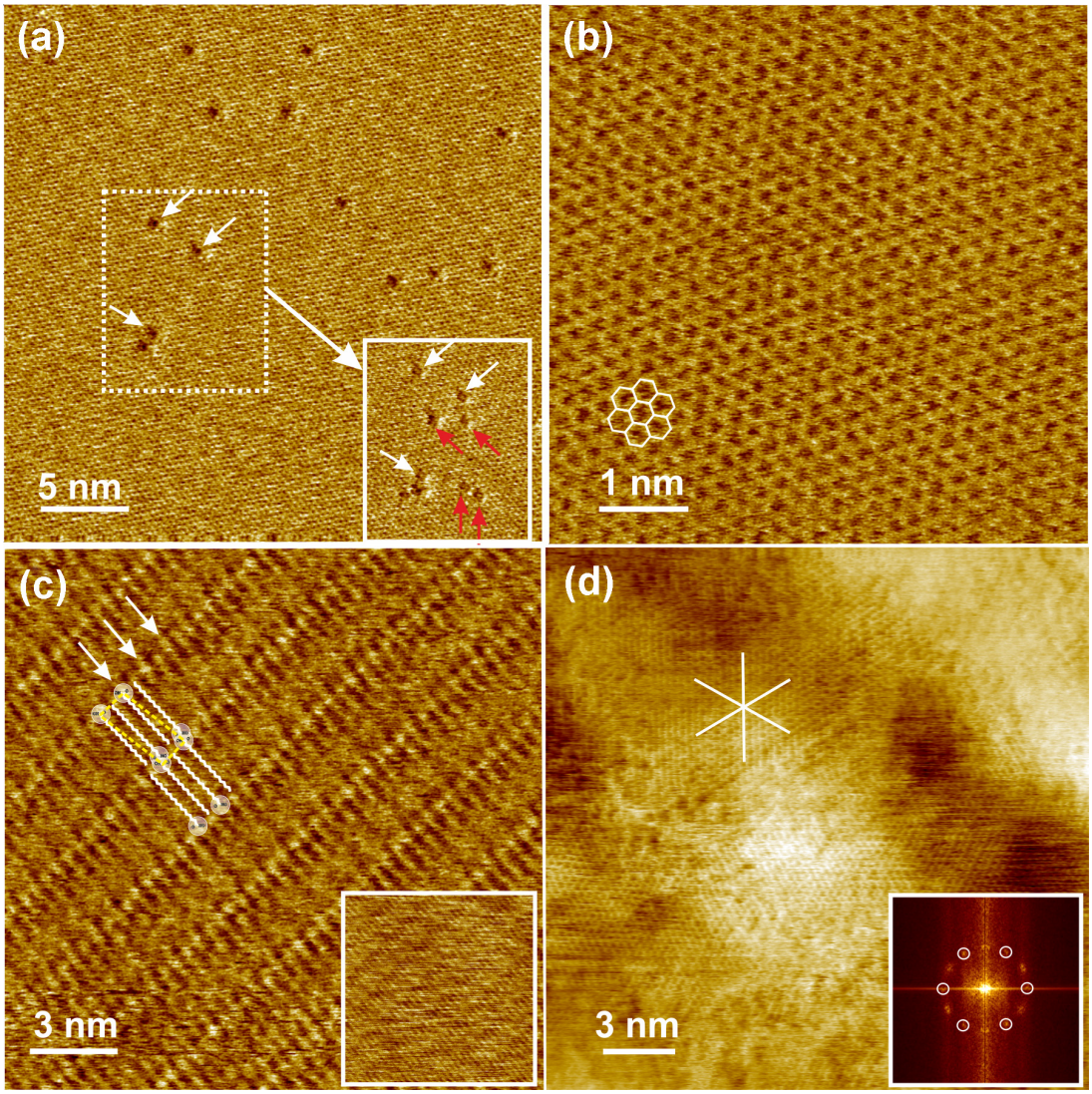

FIG. 5. High-resolution atomic force microscopy (AFM) images using higher eigenmodes on various surfaces. (a) Phase image of the cleavage plane of a natural MoS_2 crystal. The dashed rectangle highlights the area, which was subsequently tapped harder (Supplemental Material [41]); the inset (full rectangle) shows the same area after hard tapping. A few atoms were knocked off from the highlighted area. The white arrows highlight three atomic defects, which exist before and after the hard tapping; the red arrows highlight four newly created defects. A movie of knocking off the atoms is provided in the Supplemental Material [41]. (b) Phase image of a graphite surface. The white sketch in the figure the atomic scale honeycomb structure of graphene. (c) Phase image of an arachidic acid layer on a graphite surface. Inset shows height image taken simultaneously. The white sketch shows to scale the structure of an arachidic acid monolayer; the yellow dashed parallelogram shows the unit cell (adapted from Ref. [42]); the sketch was positioned to visually match the imaged pattern. (d) Height image of a MoS_2 monolayer on an amorphous quartz substrate revealing defects and domain boundaries. Inset shows the fast Fourier transform (FFT) of the image, revealing a few domains. One of the domains is highlighted with white circles in the FFT and with lines in the topography image, respectively.

close similarity of the patterns at the bottom of the images and less similarity at the top of the images. This implies that the cations are mobile, but the mobility is intrinsic and not caused by the AFM tip because the patterns are recognizable on a short time scale but change on longer time scales. The images shown in Fig. 6 prove that also imaging of the hydrophilic surfaces is possible. A discussion of the K^+ patterns and their mobility here is rather difficult due to the limited statistics; this will be done elsewhere.

To further explore the prospects on imaging stability, we performed imaging of MoS_2 at temperatures of up to 250 °C, and the imaging with subnanometer amplitudes was readily possible. Imaging of atomic scale defects was rather challenging at high temperatures due to high drifts and an instability of the cantilever coating, yet it was possible (Supplemental Material [41]). Imaging under ambient conditions was also possible albeit providing poorer image quality, possibly due to water molecules covering the surface (Supplemental Material [41]). Subsequent drying of the sample improved the image quality and allowed visualizing the atomic defects. This supports our conclusion on conservative tip-surface interactions to dominate the imaging stability since, otherwise, an ambient water meniscus forming between tip and surface is expected to affect the imaging stability.

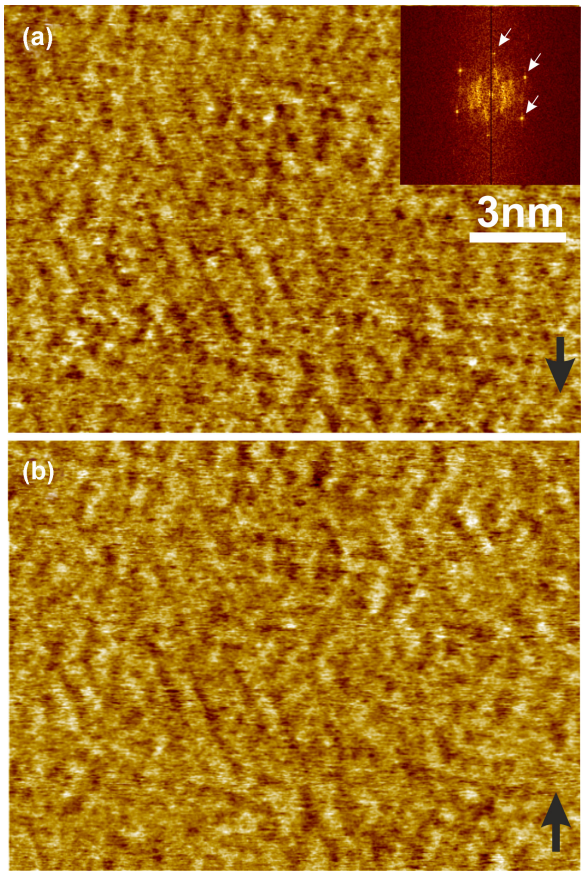

FIG. 6. (a) and (b) Two subsequently acquired phase images of muscovite mica in dry nitrogen. The images were cropped from larger images, corrected for thermal drift using the mica unit cell as a reference. Inset shows the fast Fourier transform (FFT) of the respective image; the white arrows highlight the mica unit cell frequencies. The black arrows show the slow scan directions.

Imaging with the tip oscillating with subnanometer amplitudes at a controlled distance to a surface is inherently like noncontact (nc) AFM. Therefore, we expect that the demonstrated atomic resolution can be further expanded with the nc-AFM developments; for instance, improving lateral resolution of force spectroscopy shown in Fig. 1 might allow chemical identification of atoms with the advantage of a direct measurement of the force acting between tip apex and surface atoms [Fig. 1(a)] [50,51]. Also, like nc-AFM, we expect that the resolution and reproducibility might be further improved by improving the control over the tip apex structure [52,53].

Our joint theoretical and experimental analysis leads us to the following general recipe to obtain atomic resolution in tapping mode AFM with conventional cantilevers under atmospheric pressure in gas environments. In test runs, one induces the oscillations of the cantilever with subnanometer amplitudes and investigates the stability of these oscillations without active feedback control loops under approaching the surface. For lower modes, one observes two effects: the amplitude collapse and a sharp phase change, both due to leaving the resonance domain. These two effects cannot be compensated by the feedback control loops, which makes these modes unsuitable for obtaining atomic resolution. Higher modes with much higher effective elastic constants show only gradual changes in phase and will universally make atomic resolution possible. If the atomic structure is not resolved under corresponding conditions with an atomically sharp tip, one can assume that the corresponding surface does not have a stable atomic structure (e.g., atoms or molecules covering the surface are mobile).

V. CONCLUSIONS

We showed that the common instabilities of subnanometer amplitudes of conventional cantilevers excited on their first eigenmodes are due to the fact that, upon interaction with the surface, the eigenfrequencies of the cantilevers shift out of resonance. Selecting appropriately high effective spring constants of high eigenmodes allows us to sense arbitrarily steep short-range forces. The combination of the high effective elastic constant of a higher mode with the high flexibility of the whole cantilever provides experimental advantages compared with the use of stiff cantilevers, relaxing the necessity for the precise tip-surface distance control. As a result, imaging of solid surfaces with subnanometer amplitudes in gas environments should be universally possible by exciting cantilevers at high eigenmodes.

We demonstrate imaging of a few different surfaces with cantilevers oscillating with subnanometer amplitudes. We demonstrate furthermore that the enhanced amplitude stability of high eigenmodes allows us to image knocking off atoms by tapping surfaces harder, indicating potential for atomically resolved lithography. Even more, the high stability and low noise of high eigenmodes allows atomic resolution at elevated temperatures. Obtaining atomically resolved images at elevated temperatures is of potential interest for research of phase transitions.

We expect that imaging surfaces with tapping mode force microscopy at high cantilever eigenmodes exhibiting resolutions down to atomic features in variable gaseous environments and temperatures with commonly available instruments and cantilevers will advance our understanding of surface-related phenomena.

ACKNOWLEDGMENTS

The authors thank S. Sadofev (Humboldt-Universität zu Berlin) for providing a sample of MoS_2 monolayer grown on an amorphous quartz substrate. This paper was supported by Deutsche Forschungsgemeinschaft (Projektnummer 182087777-SFB 951, S.K. and J.P.R.), the Alexander von Humboldt Foundation (C.-A.P.), and the Cluster of Excellence "Matters of Activity. Image Space Material" under Germany's Excellence Strategy EXC 2025 (J.P.R.).

APPENDIX A: MATERIALS AND METHODS

To acquire force spectroscopy curves, the cantilever was oscillated with ∼0.8 nm amplitude, being driven at its first, second, and third eigenmode frequencies, upon approaching and then retracting from a molybdenum disulfide (MoS_2) surface. The measurements were performed on a freshly cleaved sample in dry nitrogen. The AFM tip was plasma-cleaned to

remove possible organic contaminations. This experimental design minimizes the probability of formation of molecular meniscus between tip and surface, simplifying the discussion of the curves. The cantilever was tuned to one of the resonances with the tip retracted from the surface (Fig. 1). The curves were acquired (1) with no active feedback control loops (Fig. 1) and (2) with active amplitude and phase feedback control loops (Fig. 2). In the second case, the phase feedback control loop kept the phase shift between excitation and tip oscillation constant, thereby presumably keeping the excitation on the resonance with the cantilever, and the amplitude feedback control loop adjusted excitation to keep the amplitude constant. The curves shown in Figs. 1 and 2 are representative examples. Similar curves were reproduced with >10 different cantilevers.

Molybdenum disulfide (MoS_2, natural crystal, 2D Semiconductors Inc.) and highly oriented pyrolytic graphite (HOPG, Momentive Performance Inc.) were fixed onto metal sample holders with double-sided adhesive tape. The samples were cleaved under ambient conditions before imaging. A layer of arachidic acid was deposited onto a freshly cleaved HOPG surface by spin-coating its solution in chloroform under ambient conditions. The samples were placed into AFM sample cell (Cypher-ES, Asylum Research Oxford Instruments Inc.). The instrument was equipped with a standard laser module with 10 × 30 μm nominal spot size for cantilever deflection sensing. The cell was then dried with a flow of dry nitrogen (Linde group, 99.999% purity as specified by the manufacturer), unless specified. Imaging was performed in AM mode, also called tapping mode, typically using photothermal excitation of cantilevers. That is, all images were acquired with constant excitation amplitudes and frequencies. The excitation frequencies were set to match the resonances of free oscillating cantilevers. Reported images were made with the following cantilevers: three different qp-fast cantilevers (Nanosensors) with the first eigenmodes at ∼250, 420, and 800 kHz were driven at their third (∼4.4 MHz), third (∼7.4 MHz), and second (∼5 MHz) eigenmodes, respectively; NSC15 cantilevers (Mikromasch) with the first eigenmode at ∼325 kHz were driven at their third eigenmode (∼5.7 MHz); AD-40-SS cantilevers (Adama Innovations) with the first eigenmode at ∼160 kHz were driven at either their third (∼2.8 MHz), fourth (∼5.5 MHz), or fifth (∼9 MHz) eigenmodes. The AD-40-SS cantilevers had a single-crystal diamond tip. Amplitude sensitivities were not estimated for all cantilevers used for imaging. Instead, at least one cantilever of each type used for imaging was calibrated. Imaging conditions were individually optimized for each cantilever. Optimal amplitudes were roughly <1 nm, assuming similar amplitude sensitivities across the same cantilever types. The amplitude sensitivities were estimated with the combination of thermal tuning and Sader's methods as implemented in the "GetReal" calibration procedure (Asylum Research Oxford Instruments Inc.) [54]. Deflections in nanometers and then forces for all eigenmodes in Figs. 1 and 2 were calculated using the first eigenmode amplitude sensitivity and effective spring constant, respectively. For the calculations of the forces, the deflection curves were shifted along the y axis to match zero with the baseline. All cantilevers, unless indicated, were cleaned with air plasma with a Zepto instrument (Diener electronics Inc.) at 50% power for 1 min. The treatment possibly removed organic contaminations from the tip surface, improving thereby the image quality, and it possibly also modified the tip apex functionalization contributing to phase contrasts. For imaging of the mica surface, cantilevers were treated with Ar plasma with the same instrument, and settings following the methodology suggested in Ref. [55]. The images were typically acquired at line scan speeds between 3 and 20 Hz and resolutions of either 512 × 512 or 1024 × 1024 pixels. The images were processed with SPIP (Image Metrology). The images were typically line flattened by subtracting either zero or the first-order polynomials.

The raw image data are available from the corresponding authors on reasonable request.

APPENDIX B: THE ORTHOGONALITY OF EIGENMODES OF UNDAMPED CANTILEVER WITHOUT DRIVING

In this Appendix, we consider the orthogonality and the normalization of eigenfunctions of Eq. (7). Denoting two distinct solutions of the eigenvalue problem in Eq. (6) by $\psi_m(\kappa, x)$ and $\psi_n(\kappa, x)$, we can write

$$\frac{d^4\psi_m(\kappa,x)}{dx^4} = \beta_m^4\psi_m(\kappa,x); \quad 0 < x < L, \tag{B1}$$

$$\frac{d^4\psi_n(\kappa,x)}{dx^4} = \beta_n^4\psi_n(\kappa,x); \quad 0 < x < L. \tag{B2}$$

Next, we multiply Eqs. (B1) and (B2) by $\psi_n(\kappa, x)$ and $\psi_m(\kappa, x)$, respectively, integrate by parts over the domain $0 < x < L$ and, further, subtract the modified Eq. (B2) from the modified Eq. (B2). We finally obtain

$$\begin{aligned}\left(\beta_m^4 - \beta_n^4\right)\int_0^L \psi_m(\kappa,x)\psi_n(\kappa,x)dx \\ = \left[\psi_n(\kappa,x)\frac{d^3\psi_m(\kappa,x)}{dx^3}\right]_0^L - \left[\frac{d\psi_n(\kappa,x)}{dx}\frac{d^2\psi_m(\kappa,x)}{dx^2}\right]_0^L \\ - \left[\psi_m(\kappa,x)\frac{d^3\psi_n(\kappa,x)}{dx^3}\right]_0^L + \left[\frac{d\psi_m(\kappa,x)}{dx}\frac{d^2\psi_n(\kappa,x)}{dx^2}\right]_0^L.\end{aligned} \tag{B3}$$

For the system with boundary conditions in Eqs. (3) and (4), the right-hand side of Eq. (B3) vanishes, and this equation reduces to

$$\left(\beta_m^4 - \beta_n^4\right)\int_0^L \psi_m(\kappa,x)\psi_n(\kappa,x)dx = 0. \tag{B4}$$

Since $\psi_m(\kappa, x)$ and $\psi_n(\kappa, x)$ are eigenfunctions corresponding to distinct eigenvalues $\beta_m^4 \neq \beta_n^4$, for $m \neq n$, we obtain

$$\int_0^L \psi_m(\kappa,x)\psi_n(\kappa,x)dx = 0, \quad m \neq n. \tag{B5}$$

Thus, eigenfunctions $\psi_m(\kappa, x)$ and $\psi_n(\kappa, x)$ are orthogonal. When $m = n$, the integral in Eq. (B5) is positive except for the case of the trivial solution, which is of no interest. Hence,

we can normalize the natural modes by writing

$$\frac{1}{L}\int_0^L \chi(\kappa)\psi_m(\kappa,\ x)\psi_n(\kappa,x)dx\ = \delta_{mn}, \quad m,n = 1,2,\ldots \tag{B6}$$

where δ_{mn} is the Kronecker delta. The function $\chi(\kappa)$ (a normalization factor depending on κ) is chosen so that the condition in Eq. (B6) is satisfied, and $\chi(\kappa) = 1$ for $\kappa \to 0$ and $\kappa \to \infty$ in the case of the very soft and the very stiff spring, respectively. Thus, the eigenfunctions $\psi(\kappa, x)$ in Eq. (7) for a given set of boundary conditions in Eqs. (3) and (4) form an orthogonal set and are normalized as in Eq. (B6). The natural modes satisfying Eq. (B6) are referred to as normal modes in the main text.

[1] G. Binnig, C. F. Quate, and C. Gerber, Atomic Force Microscope, Phys. Rev. Lett. **56**, 930 (1986).

[2] F. J. Giessibl, Atomic force microscopy in ultrahigh vacuum, Japan. J. Appl. Phys. **33**, 3726 (1994).

[3] F. Ohnesorge and G. Binnig, True atomic resolution by atomic force microscopy through repulsive and attractive forces, Science **260**, 1451 (1993).

[4] Y. Martin, C. C. Williams, and H. K. Wickramasinghe, Atomic force microscope-force mapping and profiling on a sub 100-Å scale, J. Appl. Phys. **61**, 4723 (1987).

[5] F. J. Giessibl, Atomic resolution of the silicon (111)-(7 × 7) surface by atomic force microscopy, Science **267**, 68 (1995).

[6] R. Erlandsson, L. Olsson, and P. Mårtensson, Inequivalent atoms and imaging mechanisms in ac-mode atomic-force microscopy of Si(111)7 × 7, Phys. Rev. B **54**, R8309 (1996).

[7] F. J. Giessibl, AFM's path to atomic resolution, Mater. Today **8**, 32 (2005).

[8] K. Voïtchovsky, J. J. Kuna, S. A. Contera, E. Tosatti, and F. Stellacci, Direct mapping of the solid-liquid adhesion energy with subnanometre resolution, Nat. Nanotechnol. **5**, 401 (2010).

[9] F. J. Giessibl, The qPlus sensor, a powerful core for the atomic force microscope, Rev. Sci. Instrum. **90**, 011101 (2019).

[10] Y. Gan, Atomic and subnanometer resolution in ambient conditions by atomic force microscopy, Surf. Sci. Rep. **64**, 99 (2009).

[11] R. C. Savage, N. Mullin, and J. K. Hobbs, Molecular conformation at the crystal-amorphous interface in polyethylene, Macromolecules **48**, 6160 (2015).

[12] N. Mullin and J. K. Hobbs, Direct Imaging of Polyethylene Films at Single-Chain Resolution with Torsional Tapping Atomic Force Microscopy, Phys. Rev. Lett. **107**, 197801 (2011).

[13] M. Kocun, A. Labuda, W. Meinhold, I. Revenko, and R. Proksch, Fast, high resolution, and wide modulus range nanomechanical mapping with bimodal tapping mode, ACS Nano **11**, 10097 (2017).

[14] C. A. J. Putman, K. O. Van Der Werf, B. G. De Grooth, N. F. Van Hulst, and J. Greve, Tapping mode atomic force microscopy in liquid, Appl. Phys. Lett. **64**, 2454 (1994).

[15] Q. Zhong, D. Inniss, K. Kjoller, and V. B. Elings, Fractured polymer/silica fiber surface studied by tapping mode atomic force microscopy, Surf. Sci. **290**, L688 (1993).

[16] D. S. Wastl, A. J. Weymouth, and F. J. Giessibl, Optimizing atomic resolution of force microscopy in ambient conditions, Phys. Rev. B **87**, 245415 (2013).

[17] D. S. Wastl, Ambient atomic resolution atomic force microscopy with qPlus sensors: Part 1, Microsc. Res. Tech. **80**, 50 (2017).

[18] K. Pürckhauer, D. Kirpal, A. J. Weymouth, and F. J. Giessibl, Analysis of airborne contamination on transition metal dichalcogenides with atomic force microscopy revealing that sulfur is the preferred chalcogen atom for devices made in ambient conditions, ACS Appl. Nano Mater. **2**, 2593 (2019).

[19] K. Pürckhauer, S. Maier, A. Merkel, D. Kirpal, and F. J. Giessibl, Combined atomic force microscope and scanning tunneling microscope with high optical access achieving atomic resolution in ambient conditions, Rev. Sci. Instrum. **91**, 083701 (2020).

[20] K. Pürckhauer, A. J. Weymouth, K. Pfeffer, L. Kullmann, E. Mulvihill, M. P. Krahn, D. J. Müller, and F. J. Giessibl, Imaging in biologically-relevant environments with AFM using stiff qPlus sensors, Sci. Rep. **8**, 9330 (2018).

[21] D. S. Wastl, A. J. Weymouth, and F. J. Giessibl, Atomically resolved graphitic surfaces in air by atomic force microscopy, ACS Nano **8**, 5233 (2014).

[22] Y. Yamada, T. Ichii, T. Utsunomiya, and H. Sugimura, Simultaneous detection of vertical and lateral forces by bimodal AFM utilizing a quartz tuning fork sensor with a long tip, Jpn. J. Appl. Phys. **58**, 095003 (2019).

[23] H. Ooe and T. Arai, Layer-by-layer dissolution and recovery of KBr(001) surfaces covered with a nanometer-thick water film caused by a pressing tip controlled by frequency modulation atomic force microscopy, Appl. Phys. Express **12**, 115002 (2019).

[24] M. K. Rehmann, Y. B. Kalyoncu, M. Kisiel, N. Pascher, F. J. Giessibl, F. Müller, K. Watanabe, T. Taniguchi, E. Meyer, M.-H. Liu, and D. M. Zumbühla, Characterization of hydrogen plasma defined graphene edges, Carbon **150**, 417 (2019).

[25] D. S. Wastl, M. Judmann, A. J. Weymouth, and F. J. Giessibl, Atomic resolution of calcium and oxygen sublattices of calcite in ambient conditions by atomic force microscopy using qPlus sensors with sapphire tips, ACS Nano **9**, 3858 (2015).

[26] T. Fukuma, Y. Ueda, S. Yoshioka, and H. Asakawa, Atomic-Scale Distribution of Water Molecules at the Mica-Water Interface Visualized by Three-Dimensional Scanning Force Microscopy, Phys. Rev. Lett. **104**, 016101 (2010).

[27] V. V. Korolkov, I. G. Timokhin, R. Haubrichs, E. F. Smith, L. Yang, S. Yang, N. R. Champness, M. Schröder, and P. H. Beton, Supramolecular networks stabilise and functionalise black phosphorus, Nat. Commun. **8**, 1385 (2017).

[28] V. V. Korolkov, M. Baldoni, K. Watanabe, T. Taniguchi, E. Besley, and P. H. Beton, Supramolecular heterostructures formed by sequential epitaxial deposition of two-dimensional hydrogen-bonded arrays, Nat. Chem. **9**, 1191 (2017).

[29] V. V. Korolkov, A. Summerfield, A. Murphy, D. B. Amabilino, K. Watanabe, T. Taniguchi, and P. H. Beton, Ultra-high resolution imaging of thin films and single strands of polythiophene using atomic force microscopy, Nat. Commun. **10**, 1537 (2019).

[30] U. Rabe, K. Janser, and W. Arnold, Vibrations of free and surface-coupled atomic force microscope cantilevers: theory and experiment, Rev. Sci. Instrum. **67**, 3281 (1996).

[31] J. Kokavecz and A. Mechler, Spring constant of microcantilevers in fundamental and higher eigenmodes, Phys. Rev. B **78**, 172101 (2008).

[32] A. San Paulo and R. García, High-resolution imaging of antibodies by tapping-mode atomic force microscopy: Attractive and repulsive tip-sample interaction regimes, Biophys. J. **78**, 1599 (2000).

[33] H. Hölscher, U. D. Schwarz, and R. Wiesendanger, Calculation of the frequency shift in dynamic force microscopy, Appl. Surf. Sci. **140**, 344 (1999).

[34] J. Melcher, S. Hu, and A. Raman, Equivalent point-mass models of continuous atomic force microscope probes, Appl. Phys. Lett. **91**, 053101 (2007).

[35] S. Morita, F. J. Giessibl, Y. Sugawara, H. Hosoi, K. Mukasa, A. Sasahara, and H. Onishi, in *Nanotribology and Nanomechanics*, edited by B. Bhushan (Springer, Berlin, Heidelberg, 2005), pp. 141.

[36] R. García and R. Pérez, Dynamic atomic force microscopy methods, Surf. Sci. Rep. **47**, 197 (2002).

[37] J. A. Turner, S. Hirsekorn, U. Rabe, and W. Arnold, High-frequency response of atomic-force microscope cantilevers, J. Appl. Phys. **82**, 966 (1997).

[38] M. Gürgöze, A. N. Doğruoğlu, and S. Zeren, On the eigencharacteristics of a cantilevered visco-elastic beam carrying a tip mass and its representation by a spring-damper-mass system, J. Sound Vib. **301**, 420 (2007).

[39] J. Freundlich, Transient vibrations of a fractional Kelvin-Voigt viscoelastic cantilever beam with a tip mass and subjected to a base excitation, J. Sound Vib. **438**, 99 (2019).

[40] D. A. Ivanov, Z. Amalou, and S. N. Magonov, Real-time evolution of the lamellar organization of poly(ethylene terephthalate) during crystallization from the melt: high-temperature atomic force microscopy study, Macromolecules **34**, 8944 (2001).

[41] See Supplemental Material at http://link.aps.org/supplemental/10.1103/PhysRevResearch.4.023149. It contains a movie showing the creation of point defects by hard tapping and additional images for several situations discussed in this paper.

[42] L. K. Thomas, A. Kühnle, S. Rode, U. Beginn, and M. Reichling, Monolayer structure of arachidic acid on graphite, J. Phys. Chem. C **114**, 18919 (2010).

[43] R. Addou, L. Colombo, and R. M. Wallace, Surface defects on natural MoS_2, ACS Appl. Mater. Interfaces **7**, 11921 (2015).

[44] R. A. Bromley, R. B. Murray, and A. D. Yoffe, The band structures of some transition metal dichalcogenides. III. Group VIA: trigonal prism materials, J. Phys. C Solid State Phys. **5**, 759 (1972).

[45] S. Barja, S. Refaely-Abramson, B. Schuler, D. Y. Qiu, A. Pulkin, S. Wickenburg, H. Ryu, M. M. Ugeda, C. Kastl, C. Chen, C. Hwang, A. Schwartzberg, S. Aloni, S.-K. Mo, D. F. Ogletree, M. F. Crommie, O. V. Yazyev, S. G. Louie, J. B. Neaton, and A. Weber-Bargioni, Identifying substitutional oxygen as a prolific point defect in monolayer transition metal dichalcogenides, Nat. Commun. **10**, 3382 (2019).

[46] J. P. Rabe and S. Buchholz, Commensurability and mobility in two-dimensional molecular patterns on graphite, Science **253**, 424 (1991).

[47] N. Mutz, T. Meisel, H. Kirmse, S. Park, N. Severin, J. P. Rabe, E. List-Kratochvil, N. Koch, C. T. Koch, S. Blumstengel, and S. Sadofev, Pulsed thermal deposition of binary and ternary transition metal dichalcogenide monolayers and heterostructures, Appl. Phys. Lett. **114**, 162101 (2019).

[48] H. K. Christenson and N. H. Thomson, The nature of the air-cleaved mica surface, Surf. Sci. Rep. **71**, 367 (2016).

[49] K. Müller and C. C. Chang, Electric dipoles on clean mica surfaces, Surf. Sci. **14**, 39 (1969).

[50] Y. Sugimoto, P. Pou, M. Abe, P. Jelinek, R. Pérez, S. Morita, and Ó. Custance, Chemical identification of individual surface atoms by atomic force microscopy, Nature (London) **446**, 64 (2007).

[51] S. P. Jarvis, A. M. Sweetman, L. Kantorovich, E. McGlynn, and P. Moriarty, in *Imaging and Manipulation of Adsorbates Using Dynamic Force Microscopy*, edited by P. Moriarty and S. Gauthier (Springer, Cham, 2015), pp. 1.

[52] F. Mohn, B. Schuler, L. Gross, and G. Meyer, Different tips for high-resolution atomic force microscopy and scanning tunneling microscopy of single molecules, Appl. Phys. Lett. **102**, 073109 (2013).

[53] L. Gross, F. Mohn, N. Moll, P. Liljeroth, and G. Meyer, The chemical structure of a molecule resolved by atomic force microscopy, Science **325**, 1110 (2009).

[54] A. Labuda, M. Kocun, M. Lysy, T. Walsh, J. Meinhold, T. Proksch, W. Meinhold, C. Anderson, and R. Proksch, Calibration of higher eigenmodes of cantilevers, Rev. Sci. Instrum. **87**, 073705 (2016).

[55] S. M. R. Akrami, H. Nakayachi, T. Watanabe-Nakayama, H. Asakawa, and T. Fukuma, Significant improvements in stability and reproducibility of atomic-scale atomic force microscopy in liquid, Nanotechnology **25**, 455701 (2014).